Investigation on the Stability and Efficiency of MAPbI$_3$ and MASnI$_3$ Thin Films for Solar Cells

Julia Marí-Guaita, Amal Bouich, Muhammad Aamir Shafi, Asmaa Bouich, and Bernabé Marí

Hybrid organic–inorganic halides are considered as outstanding materials when used as the absorber layer in perovskite solar cells (PSCs) because of its efficiency, relieve of fabrication and low-cost materials. However, the content of lead (Pb) in the material may origin a dramatic after effect on human's health caused by its toxicity. Here, we investigate replacing the lead in MAPbI$_3$ with tin (Sn) to show its influence on the growth of the film nucleation and stability of the solar device based on MASnI$_3$. By analysing the manufactured perovskite films by scanning electron microscopy (SEM), transmission electron microscopy (TEM), X-ray diffraction (XRD), UV–visible absorption, photoluminescence (PL) and atomic force microscopy (AFM), the properties of the thin films when lead is replaced by tin are reported. The simulation run for the case of MAPbI$_3$ is reported, where $V_{oc} = 0.856$ V, $J_{sc} = 25.65$ mA cm^{-2}, FF $= 86.09\%$, and ETA $= 18.91\%$, and for MASnI$_3$, $V_{oc} = 0.887$ V, $J_{sc} = 14.02$ mA cm^{-2}, FF $= 83.72\%$, and ETA $= 10.42\%$. In perovskite-based devices using MASnI$_3$ as absorber, it was found to be more stable despite of its lower efficiency, which could be improved by enhancing the bandgap alignment of MaSnI$_3$. The results of this paper also allow the development of a new, reliable production system for PSCs.

1. Introduction

Perovskite materials possess excellent optical and electrical properties, such as a direct bandgap ranging from 1.5 to 2.3 eV and the potential to transport electrons and holes.[1–3] For manufacturing perovskite thin films with good morphology and high quality, various low-cost techniques have been used. Among these techniques, spin coating with one-step process is usually used as it is easy to control and quick to produce.[4,5] Also, the two-step process is widely used due to its ease of control for the preparation of perovskite thin layers.[6] Other PSCs' manufacturing techniques are the two-step vapor-assisted deposition, which is advantageous for controlling the thin film morphology, thickness, and grain size,[7] and thermal vapor deposition normally used to manufacture films with consistent thickness.

Indeed, the highest conversion efficiency in PSCs is reached when MAPbI$_3$ is used as an absorber. Moreover, the content of lead (Pb) in the material may lead to a dramatic aftereffect on human health caused by its toxicity. This is why the required study of substituting the lead in MAPbI$_3$ by tin (Sn) is highly suitable and must be done. In the article, we report on the influence on the growth of film nucleation and stability of the solar device based on MASnI$_3$ perovskite (instead of MAPbI$_3$ absorbers), having elaborated both absorbers with the same one-step deposition technique. This technique exhibits wide-scale manufacturing for PSCs with high performance. Typically, the fabrication of the device is associated with the regulation of the surface shape and the capability to be developed scaled-up. The surface morphology has shown to be highly controllable and that it is the primary factor influencing the efficiency of PSCs. For this reason, many techniques and treatments for PSCs have been revised to improve the surface uniformity and the perovskite crystal formation.

In this work, we looked at the impact of replacing Pb by Sn on the properties of perovskite MAPbI$_3$ thin film. We report complex changes of the device by observing the morphology and the composition of the films. The obtained perovskite devices were characterized by X-ray diffraction (XRD), scanning electron microscopy (SEM), atomic force microscopy (AFM), transmission electron microscopy (TEM), photoluminescence (PL), and UV–vis absorption analysis to inquire into the electrical and optical properties of the deposited films and the performance of solar cells which were estimated by SCAPS simulator.[8]

2. Perovskite Manufacture

Perovskite absorbers ABX$_3$, where A $=$ methylammonium (MA), B $=$ (Pb or Sn), and X $=$ Iodide (I), were manufactured employing different materials purchased from Sigma-Aldrich and Alfa

J. Marí-Guaita, A. Bouich, A. Bouich, B. Marí
Institut de Disseny, Fabricació i Producció Automatizada
Universitat Politècnica de València
València 46022, Spain
E-mail: bmari@fis.upv.es

A. Bouich
Department of Computer Science Engineering
Ibn Tofail University
Kenitra 14000, Morocco

M. A. Shafi
Department of Electrical Engineering
COMSATS University Islamabad
Islamabad 45550, Pakistan

The ORCID identification number(s) for the author(s) of this article can be found under https://doi.org/10.1002/pssa.202100664.

Caesar. Specifically, methylammonium iodide (MAI), thin II iodide 99% (SnI_2), and lead iodide (PbI_2) were used as precursors, and N-dimethylformamide (DMF) and dimethyl sulfoxide (DMSO) were used as solvents.

First, the prepared solutions of $MAPbI_3$ and $MASnI_3$ were dropped onto fluorine-dope tin oxide (FTO) glass substrates. The FTO glass was spun at 4000 rpm for 50 s during the dripping of the perovskite solution and the addition of toluene as antisolvent. Later, the samples were annealed at 60 °C for 5 min, followed by an annealing at 100 ºC for 10 min. **Figure 1** shows a diagram of the elaboration process carried out.

3. Characterization Techniques

The structural properties of the thin films were examined by XRD with RIGAKU Ultima IV diffractometer using Cu Kα radiation ($\lambda = 1.5418$ Å). SEM was used to examine the surface morphology of the perovskite layers using 1.5 kV at different magnifications. AFM measurements were performed using Nano Surf with a voltage cell from -1.5 to 1.5 V at a scan rate of 0.5 Hz. TEM (JEO-JEM-1010) analysis was carried out with 2.5 kV at different magnifying tools. UV–vis absorption analysis was made with a Si charge couple device, and PL emission was excited with a 405 nm semiconductor laser. The output parameters of the solar cell, namely, in the short-circuit current density (J_{sc}), the open-circuit voltage (V_{oc}), the fill factor (FF), and the efficiency (η), were assessed by SCAPS simulator.

4. Results and Discussion

The XRD scanning of $MAPbI_3$ and $MASnI_3$ thin films (**Figure 2**) reveals various diffractions peaks located at 14°, 28°, and 52° matching the characteristics peaks of the perovskite materials (110), (220), and (303) respectively. Previously published structures of $MAPbI_3$[9] are in good agreement with the patterns of this work. Furthermore, it was observed that the replacement of Pb by Sn leads to an increase in the intensity of the peak (110). All perovskite films form a tetragonal crystal structure with the space group $I4/mcm$.

Table 1. The structural parameters of $MAPbI_3$ and $MaSnI_3$ thin films.

Sample ID	Grain size [nm]	Roughness [nm]	Dislocation density [10^{-05} nm^{-1}]	Lattice strain (ϵ)
$MaSnI_3$	403	46.7	0.62	0.39
$MaPbI_3$	302	37.0	1.11	0.37
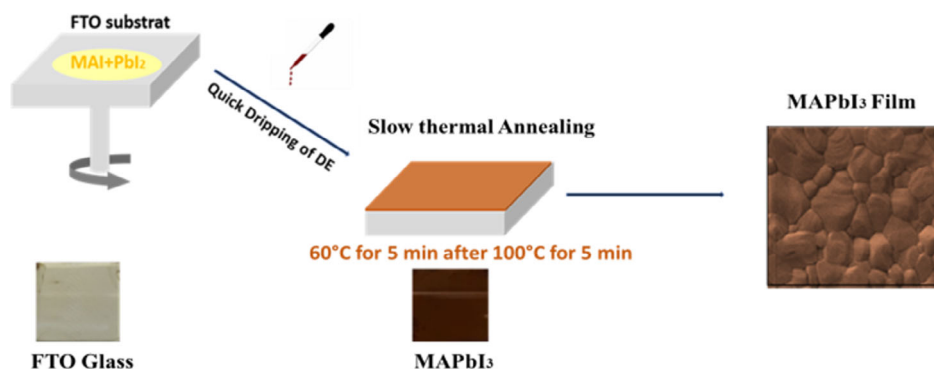
Figure 1. Elaboration process of $MAPbI_3$ and $MASnI_3$ thin films.
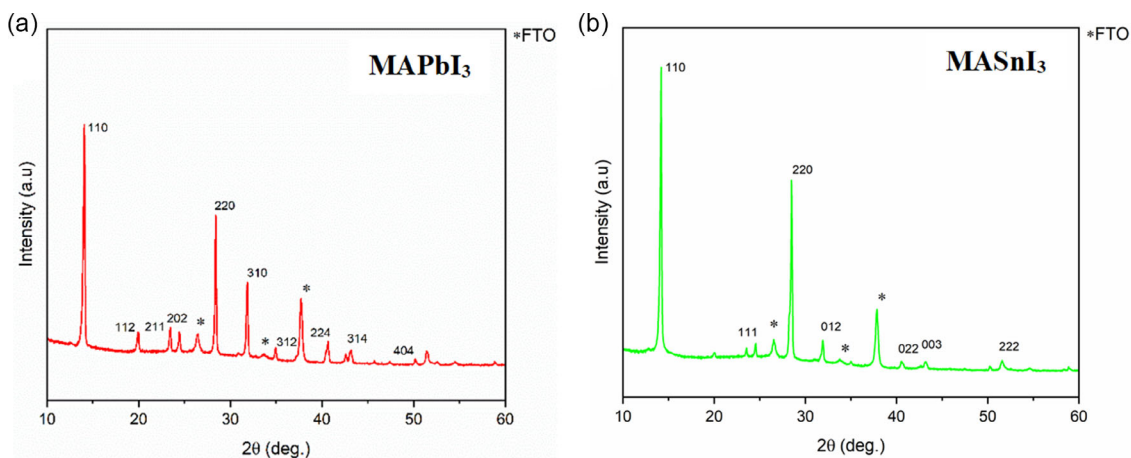

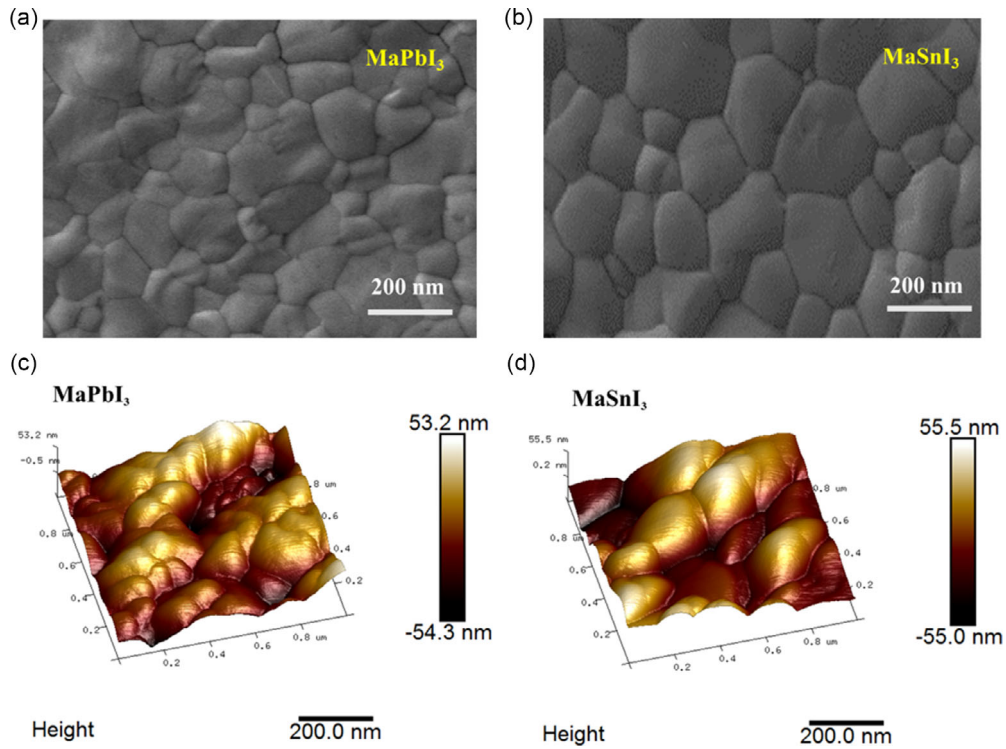**Figure 2.** XRD patterns of $MAPbI_3$ and $MASnI_3$.

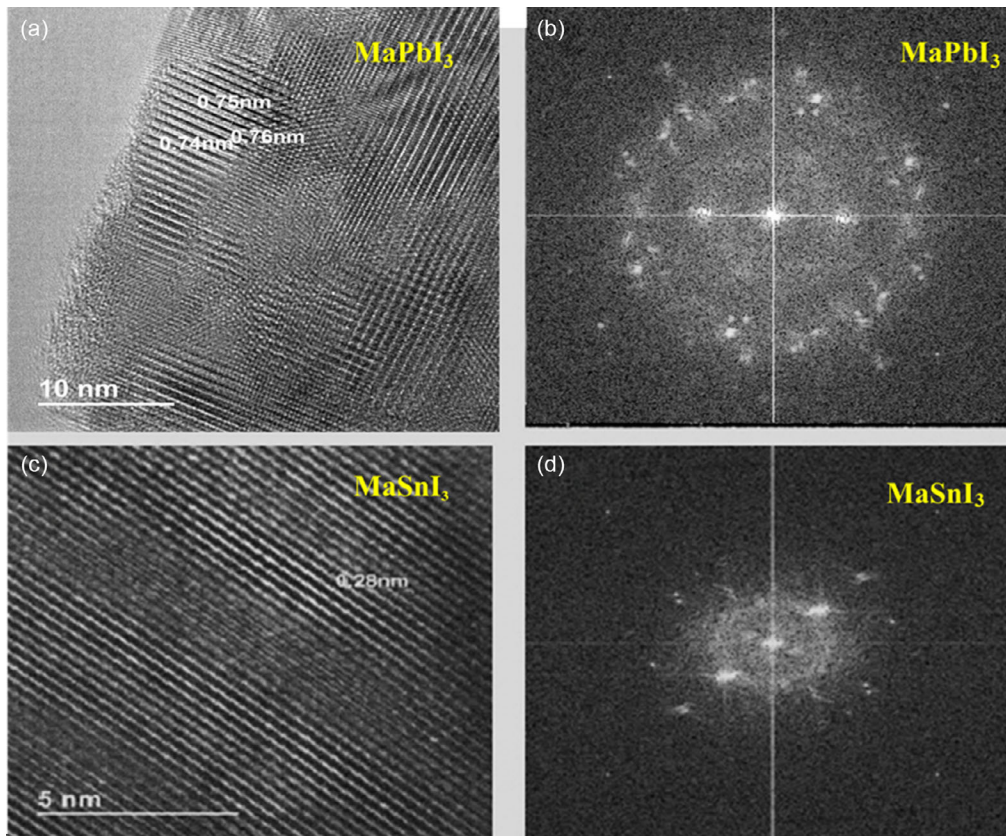**Figure 3.** SEM images of a) MaPbI$_3$ and b) MASnI$_3$. AFM images of c) MaPbI$_3$ and d) MASnI$_3$.

Figure 4. a,c) High resolution transmission electron microscopy images of MAPbI$_3$ and MASnI$_3$, respectively. b,d) SAED of MAPbI$_3$ and MASnI$_3$, respectively.

The (110) XRD peak is wider for $MASnI_3$ than for $MAPbI_3$, as revealed by the values of full width at half maximum (FWHM) for this XRD peak (FWHM (110) = 0.23 for $MASnI_3$ and FWHM (110) = 0.13 for $MaPbI_3$), which means bigger crystallite sizes for $MAPbI_3$, according to the well-known Scherrer equation.[10]

The calculated grain size, dislocation density, lattice strain, and effective lattice strain data are represented in **Table 1**. The grain size for $MASnI_3$ (403 nm) thin films was found to have a substantial bigger grain size than $MAPbI_3$, which was 302 nm. So, according to XRD and AFM analysis, when Pb is replaced by Sn, grain sizes increase even if crystallite sizes decrease. Further, dislocation density and effective lattice strain have been calculated to have an idea about scarcity and deformations of the grains in the film.

Figure 3a,b shows SEM images of $MAPbI_3$ and $MASnI_3$, and the surface morphology of both thin films was smooth and contained random grain boundaries. Furthermore, $MASnI_3$ showed improvement of the surface morphology like previously reported investigations.[11,12] It can be clearly observed from the homogeneity of the surface that $MASnI_3$ had large grain size around 403 nm, whereas for $MAPbI_3$ film, the grain size was about 302 nm. Also, the addition of antisolvent toluene, which evaporates the solvent and therefore creates supersaturation to speed up the crystallization process, resulted in excellent film development. Moreover, temperature annealing treatment had a significant impact on the surface of the films. Results indicate that when annealing temperature increases, the crystal as well as the grain size grow considerably. Figure 3c,d shows the AFM analysis of $MAPbI_3$ and $MASnI_3$ over a 2 μm × 2 μm region. Computed roughness of $MAPbI_3$ was 37.0 nm, and when Pb was replaced by Sn, roughness was 46.7 nm (Table 1). The surface of $MASnI_3$ is rougher due to the huge size of hills and troughs.

TEM examinations of $MASnI_3$ and $MAPbI_3$ thin films with lattice fringe spacings of 0.28 and 0.75 nm, respectively, corresponding to (110) or (220) of the tetragonal perovskite phases, are shown in Figure 3a,c. Figure 3 exhibits the selected-area electron diffraction (SAED) spectrum and revealed that $MAPbI_3$ and $MASnI_3$ thin films are polycrystalline; validated findings (**Figure 4**).[13–15]

PL measurement was recorded in the range of 500–1100 nm, as represented in **Figure 5**. The PL peak intensity in the region of 700–900 nm is in good agreement with the previously reported study of $MAPbI_3$.[16] The measured intensity of the PL peak in $MAPbSn_3$ films is about 30% higher than in $MAPbI_3$ films.

It is suggested that tin can be placed at the optimal level for absorbing light. This finding also boosts the enhancement crystallinity of the perovskite thin film. The UV–vis absorption spectrum of $MAPbI_3$ and $MASnI_3$ was obtained between 400 and 900 nm. The optical bandgap was calculated through the Tauc
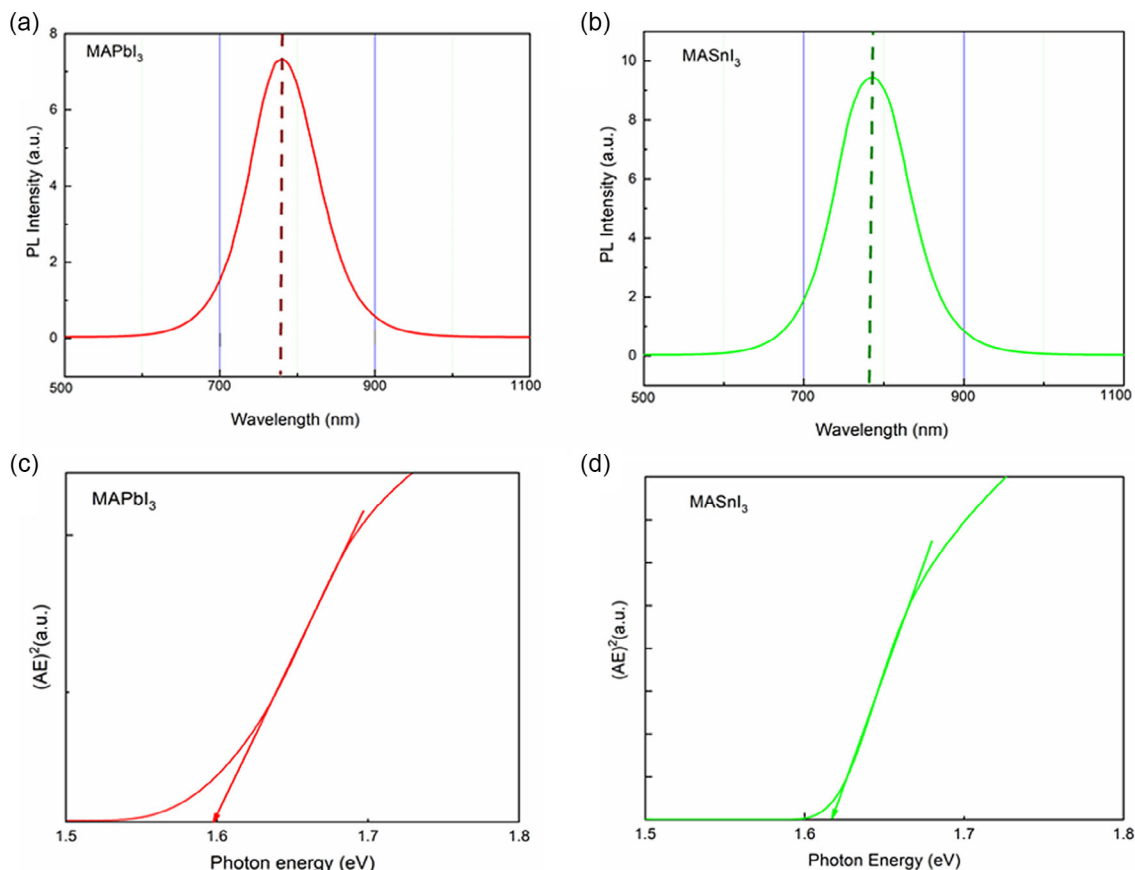

Figure 5. a) PL emission for $MAPbI_3$ perovskite thin films, b) PL emission for $MaPbI_3$ perovskite thin films, c) optical bandgap of $MAPbI_3$, and d) optical bandgap of $MASnI_3$.

Table 2. PL and optical bandgap for MAPbI$_3$ and MASnI$_3$.

Sample ID	PL		Optical absorption		Stokes shift [meV]
	λ [nm]	E_g [eV]	λ [nm]	E_g [eV]	
MaPbI$_3$	780	1.59	775	1.60	10
MaSnI$_3$	786	1.58	765	1.62	40

plot for the absorbance spectrum, from the equation $(Ah\nu)^2 = B(h\nu - E_g)$. An optical bandgap of 1.60 eV and 1.62 was found for MAPbI$_3$ and MASnI$_3$ films respectively (Figure 5c,d).[17–19] **Table 2** summarizes the optical bandgap and PL emission peaks according to PL and UV–vis absorption measurements. The energy difference between the edge of the optical absorption and the energy of the PL emission, known as Stokes shift, is found to be higher for MASnI$_3$ (40 meV) than for MAPbI$_3$ (10 meV), meaning that the bottom of the conduction band is more filled with electrons in MASnI$_3$ films.

5. Degradation Study

Environmental components like oxygen and humidity have a significant impact on the photovoltaic stability of perovskite solar devices. The degradation mechanism of methylammonium-based perovskites when exposed to the environment has been attributed to a reduction of these compounds in PbI$_2$, CH$_3$NH$_2$, and HI. To evaluate the degradation of MAPbI$_3$ and MaSnI$_3$ samples, we performed XRD, SEM, and PL measurements on fresh and 4 weeks-aged samples, kept under 60% of humidity and in the dark (**Figure 6**).
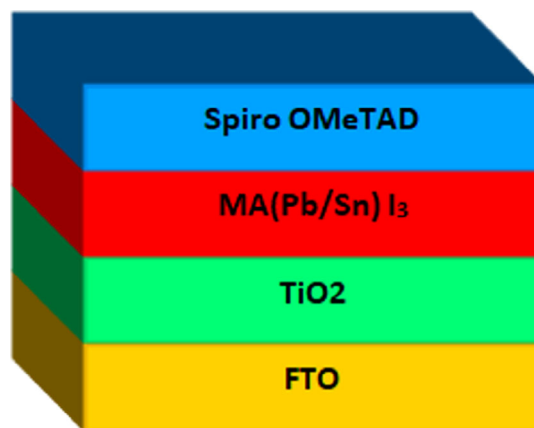

Figure 7. Schematic diagram of the proposed solar used in SCAPS.

For the 4 weeks-aged MAPbI$_3$ samples, XRD patterns reveal lesser intensity of characteristic peaks (Figure 6a) and a reduction of the intensity of PL emission (Figure 6c). In the case of 4 weeks-aged MASnI$_3$ samples, both XRD peaks and PL emission decrease in intensity, but this reduction in intensity is minor for MASnI$_3$ than for MAPbI$_3$ samples (Figure 6d,e). This fact means that MASnI$_3$ samples are more stable than MAPbI$_3$ ones. Similar results are reported in literature.[20–24] Further, SEM images (Figure 6b,e) support this finding. New grain boundaries, as presented in Figure 6b, appear in aged MAPbI$_3$ films. In the case of aged MASnI$_3$ films, some new defects consisting of pinholes and changes in the surface morphology with respect to no fresh samples (Figure 6e) are observed in SEM images. As a
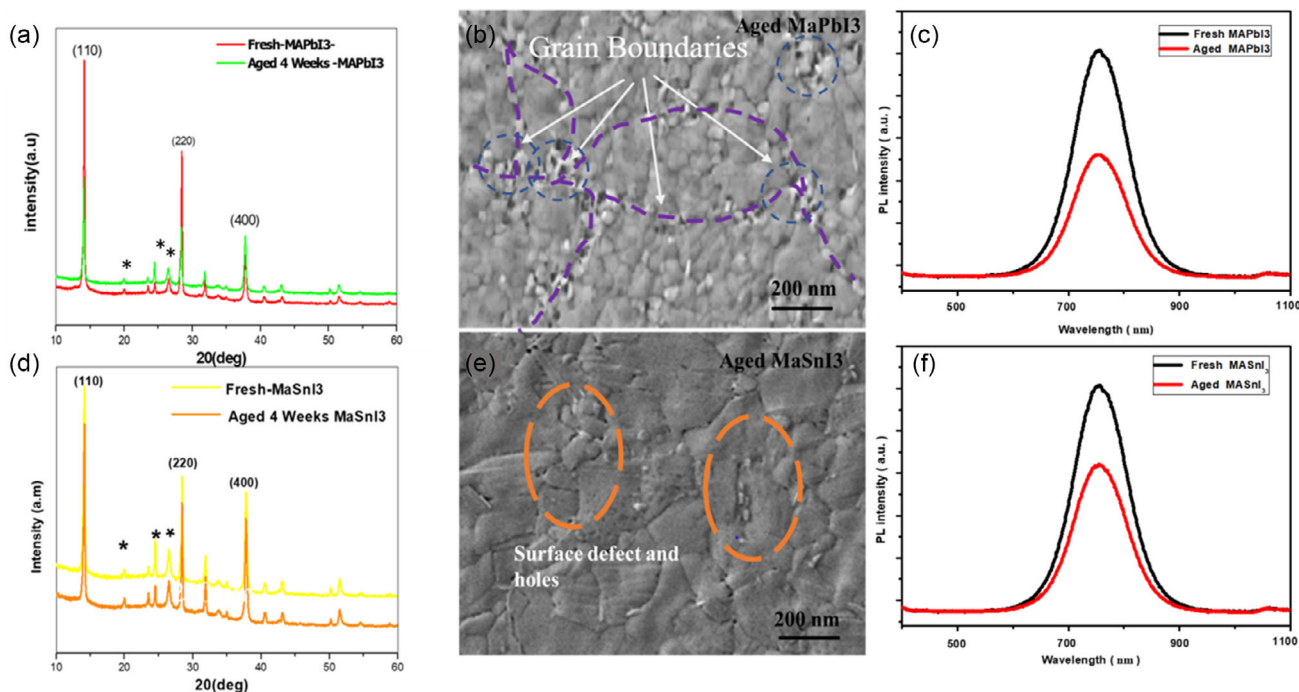

Figure 6. Degradation study of MAPbI$_3$ a) XRD pattern of the fresh and aged MAPbI$_3$ samples after 4 weeks. b) SEM image of aged MAPbI$_3$. c) PL emission of aged fresh and aged MAPbI$_3$ samples.

result, the degradation process seems to be different for both types of films.

6. Device Manufacture and Numerical Simulation

For the study of the solar cell performance, we performed the simulation of MAPbI$_3$ and MASnI$_3$-based Perovskites solar cells using SCAPS simulator software. The structure of solar spiro OMeTAD/MA(Pb/Sn)I$_3$/TiO$_2$/FTO used in the simulation is shown in the diagram (**Figure 7**).

The simulation was run two times for OMeTAD/MAPbI$_3$/TiO2/FTO and OMeTAD/MASnI$_3$/TiO$_2$/FTO proposed models separately.[25,26] **Figure 8** and **9** show the J–V and P–V characteristics curves, and from these curves we observed that MASnI$_3$-based solar cell is less efficient as compared with MAPbI$_3$ based solar cell. The bandgap of MAPbI$_3$ is more favorable for light absorption as compared with the other one.
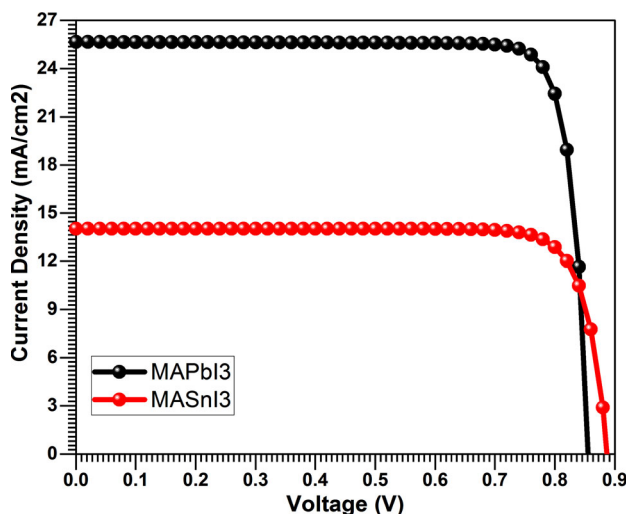
Table 3. Characteristics parameters of MAPbI$_3$ and MASnI$_3$ obtained by simulation.

Absorber	V_{oc}	J_{sc}	FF	ETA
	[V]	[mA cm^{-2}]	[%]	[%]
MAPbI$_3$	0.856	25.65	86.09	18.91
MASnI$_3$	0.888	14.02	83.72	10.42

The results of simulation are summarized in **Table 3**, where the photovoltaic characteristic parameters V_{oc} (open-circuit voltage), J_{sc} (short-circuit current density), FF, and ETA (conversion efficiency) are shown. When the simulation was run for the case of MAPbI$_3$, we find the V_{oc} of 0.856 V, J_{sc} of 25.65 mA cm^{-2}, FF of 86.09%, and ETA of 18.91%. For MASnI$_3$, we report V_{oc} of 0.888 V, J_{sc} of 14.02 mA cm^{-2}, FF of 83.72%, and ETA of 10.42%. It is worthy to notice that there is about 9% difference in the efficiencies of both devices. For Sn-based PSCs, this efficiency could be improved by enhancing the bandgap alignment of MASnI$_3$ with respect the hole transport layer and by adjusting film thickness.

To better show the differences of the photovoltaic parameters of MAPbI$_3$ and MASnI$_3$, a bar graph displaying the four photovoltaic parameters for both proposed devices is shown in **Figure 10**. This comparison shows a well-defined difference between both devices' parameters.

7. Conclusion

In summary, the use of Sn in spite of Pb to increase the stability and decrease toxicity of perovskite solar cells (PSCs) has been demonstrated. Results show a higher intensity of the characteristic peaks of perovskite when using Sn. Replacement of Pb by Sn has a significant impact on the crystallization process of
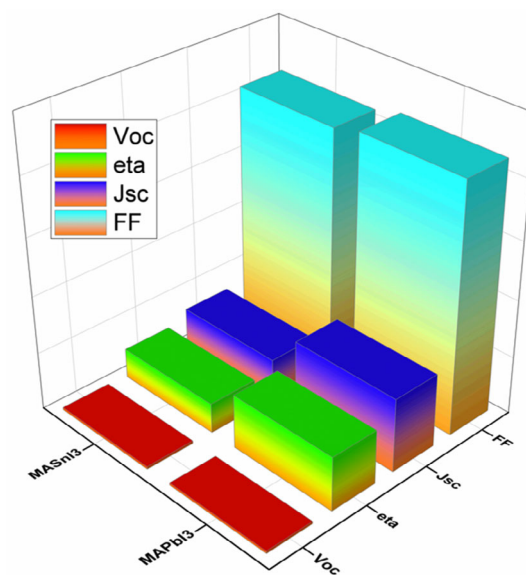

Figure 8. J–V characteristics curve for both MAPbI$_3$and MASnI$_3$.
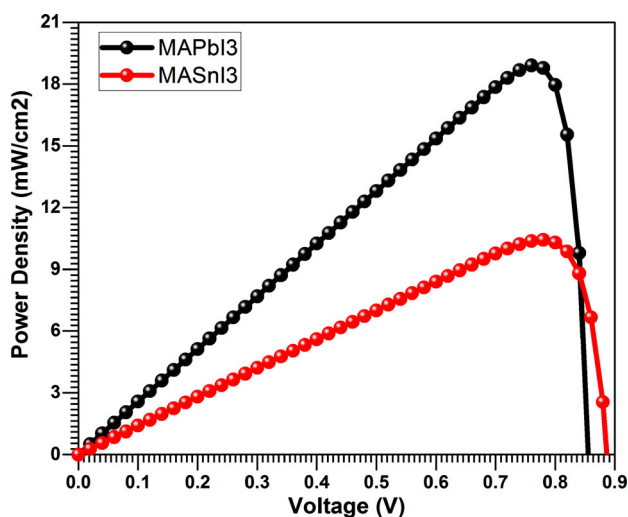
Figure 9. P–V characteristics curve for both MAPbI$_3$and MASnI$_3$.

Figure 10. Graphical comparison of characteristics parameters of MAPbI$_3$and MASnI$_3$.

perovskite materials and produces an increase in the grain size of the perovskite thin film, as seen by SEM pictures. The fact that Sn increases the grain size may result in an increase in the light absorption of the perovskite layer. Optimizing the inclusion of Sn in perovskite-based solar cells can significantly enhance stability, according to our research. Simulation was run for both films prepared. On the one hand, for $MAPbI_3$, we obtained $V_{oc} = 0.856\,V$, $J_{sc} = 25.65\,mA\,cm^{-2}$, $FF = 86.09\%$, and $ETA = 18.91\%$. On the other hand, for $MASnI_3$, we calculated $V_{oc} = 0.888\,V$, $J_{sc} = 14.02\,mA\,cm^{-2}$, $FF = 83.72\%$, and $ETA = 10.42\%$. Here, we report that there is around 9% difference in efficiencies of both devices. However, in case of Sn-based perovskite, this efficiency could be enhanced by improving the bandgap alignment of the material.

Conflict of Interest

The authors declare no conflict of interest.

Data Availability Statement

The data that support the findings of this study are available from the corresponding author upon reasonable request.

Keywords

[1] A. Bouich, S. Ullah, H. Ullah, M. Mollar, B. Marí, M. E. Touhami, *JOM* **2020**, *72*, 615.

[2] N. J. Jeon, H. Na, E. H. Jung, T. Y. Yang, Y. G. Lee, G. Kim, H.-W. Shin, S. Il Seok, J. Lee, J. Seo, *Nat. Energy* **2018**, *3*, 682.

[3] A. Bouich, S. Ullah, B. Marí, L. Atourki, M. E. Touhami, *Mater. Chem. Phys.* **2021**, *258*, 123973.

[4] J. H. Im, H. S. Kim, N. G. Park, *Appl. Mater.* **2014**, *2*, 081510.

[5] M. J. Carnie, C. Charbonneau, M. L. Davies, J. Troughton, T. M. Watson, K. Wojciechowski, H. Snaith, D. A. Worsley, *Chem. Commun.* **2013** *49*, 7893.

[6] D. Bi, S. J. Moon, L. Häggman, G. Boschloo, L. Yang, E. M. Johansson, M. K. Nazeeruddin, M. Grätzel, A. Hagfeldt, *RSC Adv.* **2013**, *3*, 18762.

[7] Q. Chen, H. Zhou, Z. Hong, S. Luo, H. S. Duan, H. H. Wang, Y. Liu, G. Li, Y. Yang, *J. Am. Chem. Soc.* **2013**, *136*, 622.

[8] A. Bouich, B. Hartiti, S. Ullah, H. Ullah, M. E. Touhami, D. M. F. Santos, B. Mari, *Optik* **2019**, *183*, 137.

[9] W. Kong, Z. Ye, Z. Qi, B. Zhang, M. Wang, A. Rahimi-Iman, H. Wu, *Phys. Chem. Chem. Phys.* **2015**, *17*, 16405.

[10] U. Holzwarth, N. Gibson, *Nature Nanotechnol.* **2011**, *6*, 534.

[11] Z. Xiao, Q. Dong, C. Bi, Y. Shao, Y. Yuan, J. Huang, *Adv. Mater.* **2014**, *26*, 6503.

[12] S. Luo, W. A. Daoud, *Materials* **2016**, *9*, 123.

[13] N. G. Park, *CrystEngComm* **2016**, *18*, 5977.

[14] X. Zheng, B. Chen, C. Wu, S. Priya, *Nano Energy* **2015**, *17*, 269.

[15] Q. Jeangros, M. Duchamp, J. Werner, M. Kruth, R. E. Dunin-Borkowski, B. Niesen, A. Hessler-Wyser, *Nano Lett.* **2016**, *16*, 7013.

[16] D. Liu, J. Yang, T. L. Kelly, *J. Am. Chem. Soc.* **2014**, *136*, 17116.

[17] M. Zhang, H. Yu, M. Lyu, Q. Wang, J. H. Yun, L. Wang, *Chem. Commun.* **2014**, *50*, 11727.

[18] J. J. Choi, X. Yang, Z. M. Norman, S. J. Billinge, J. S. Owen, *Nano Lett.* **2013**, *14*, 127.

[19] A. Halder, R. Chulliyil, A. S. Subbiah, T. Khan, S. Chattoraj, A. Chowdhury, S. K. Sarkar, *J. Phys. Chem. Lett.* **2015**, *6*, 3483.

[20] Z. Xie, S. Sun, Y. Yan, L. Zhang, R. Hou, F. Tian, G. G. Qin, *J. Phys. Conden. Matter* **2017**, *29*, 245702.

[21] C. C. Homes, T. Vogt, S. M. Shapiro, S. Wakimoto, A. P. Ramirez, *Science* **2001**, *293*, 673.

[22] G. Abdelmageed, L. Jewell, K. Hellier, L. Seymour, B. Luo, F. Bridges, J. Z. Zhang, S. Carter, *Appl. Phys. Lett.* **2016**, *109*, 233905.

[23] J. Li, Q. Dong, N. Li, L. Wang, *Adv. Energy Mater.* **2017**, *7*, 1602922.

[24] A. Bouich, B. Mari, L. Atourki, S. Ullah, M. E. Touhami, *JOM* **2021**, *73*, 551.

[25] X. Wu, H. Wang, Y. Song, X. Ma, Z. Zeng, J. Wu, Y. Liu, *Improving the Performance of Organic Lead-tin Laminated Perovskite Solar Cells from the Perspective of Device Simulation*, Springer **2021**.

[26] H. Alipour, A. Ghadimi, *Opt. Mater.* **2021**, *120*, 111432.